

# DFT-Based Engineering of Dirac Surface Energy in Topological-Insulator Multilayers

Takao Kosaka, Kunihiko Yamauchi\* and Tamio Oguchi

*Institute of Scientific and Industrial Research, Osaka University, 8-1 Mihogaoka, Ibaraki, Osaka 567-0047, Japan*

Aiming at the future spintronics device applications of the spin-polarized surface states in three-dimensional topological insulator, a highly insulating bulk state and a tunable Dirac cone surface state are required. Here we employ a slab model having hetero-structural  $\text{Bi}_2\text{Se}_3$ -related quintuple layers and perform first-principles simulations. Our computational results show that the Dirac-point energy can be optimally tuned by selecting an appropriate pair of materials so that the work function at the surface quintuple layer is slightly different from that at the inner quintuple layers. The ideal surface state is obtained in  $\text{Bi}_2\text{Te}_3/(\text{Bi}_2\text{Te}_2\text{Se})_4/\text{Bi}_2\text{Te}_3$  slab, in which the Fermi lines show the significant warping effect and both the in-plane and the out-of-plane components of the spin polarization emerge.

arXiv:1912.13239v1 [cond-mat.mtrl-sci] 31 Dec 2019

## 1. Introduction

A three-dimensional topological insulator (TI) exhibits the non-trivial quantum states which can be characterized by the insulating bulk states and the spin-polarized metallic surface states.<sup>1-4</sup> The latter is known to have the Dirac cone dispersion and show the spin polarized state, which has an appealing potential for future spintronics device applications. Although the highly insulating bulk state and the tunable Dirac cone in the bulk band gap are desired for the applications, many of topological insulators have been found to be metallic due to the existence of impurities and/or structural disorder. For example, in  $\text{Bi}_2\text{Se}_3$ , Se vacancies and Se anti-site defects lead to electron carrier doping in the conduction bands.<sup>5-9</sup> In  $\text{Bi}_2\text{Te}_3$ , Te (Bi) anti-site defects leads to electron (hole) carrier doping.<sup>5)6)10</sup> It has been also observed that the Dirac point is embedded in the bulk valence bands in  $\text{Bi}_2\text{Te}_3$ ,<sup>11-13</sup> which makes impossible to utilize the Dirac carrier. Recently, it has been reported that  $\text{Bi}_2\text{Te}_2\text{Se}$ <sup>14,15</sup> and  $\text{Bi}_{2-x}\text{Sb}_x\text{Te}_{3-y}\text{Se}_y$  solid solution<sup>16-18</sup> show highly bulk insulating states, because the defect formation can be suppressed by controlling the solid solution ratio in these materials. In these materials, the spin-polarized Dirac cones appear in the middle of the band gap, and therefore they are now considered as a good playground to experimentally investigate the topological surface bands. In the present study, by using first-principles calculations, we propose an alternative way to tune the Dirac-cone energy, that is, artificial stacking control of the  $\text{Bi}_2\text{Se}_3$ -related quintuple-layer slabs.

## 2. Method

### 2.1 Structural Models

Three dimensional topological insulators,  $\text{Bi}_2\text{Se}_3$ ,  $\text{Bi}_2\text{Te}_3$ ,  $\text{Bi}_2\text{Te}_2\text{Se}$  and  $\text{Sb}_2\text{Te}_3$ , crystallize in ternary tetradymite structure as shown in Fig. 1 (a). The covalently bonded quintuple layers (QLs) are weakly stacked in the ABCABC sequence through van der Waals interaction. In this study, we set up a multi-QL periodic slab model which contains two kinds of topological-insulator materials selected out of  $\text{Bi}_2\text{Se}_3$ ,  $\text{Bi}_2\text{Te}_3$ ,  $\text{Bi}_2\text{Te}_2\text{Se}$ ,  $\text{Sb}_2\text{Te}_3$  and  $\text{Sb}_2\text{Se}_3$  (Note: among them, only  $\text{Sb}_2\text{Se}_3$  is a trivial insulator). The multi-QL se-

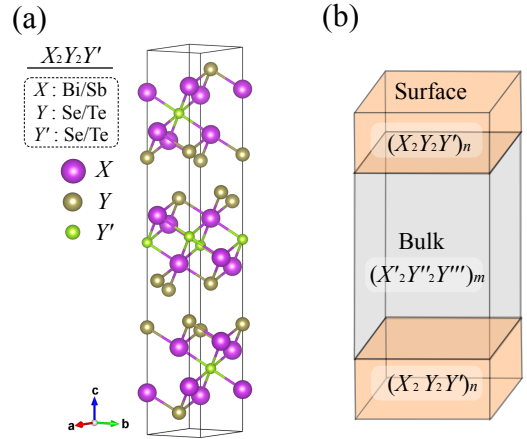


**Fig. 1.** (a) Crystal structure of tetradymite chalcogenides  $X_2Y_2Y'$ , such as  $\text{Bi}_2\text{Se}_3$  ( $X = \text{Bi}$ ,  $Y = Y' = \text{Se}$ ),  $\text{Bi}_2\text{Te}_3$  ( $X = \text{Bi}$ ,  $Y = Y' = \text{Te}$ ),  $\text{Bi}_2\text{Te}_2\text{Se}$  ( $X = \text{Bi}$ ,  $Y = \text{Te}$ ,  $Y' = \text{Se}$ ),  $\text{Sb}_2\text{Te}_3$  ( $X = \text{Sb}$ ,  $Y = Y' = \text{Te}$ ) and  $\text{Sb}_2\text{Se}_3$  ( $X = \text{Sb}$ ,  $Y = Y' = \text{Se}$ ), in a hexagonal setting. (b) A schematic structure of the hetero-structural multi-QL slab.

quence is described as  $(X_2Y_3)_n/(X_2Y_3)_m/(X_2Y_3)_n$  ( $X = \text{Bi}$  or  $\text{Sb}$ , and  $Y = \text{Te}$  or  $\text{Se}$ ) as shown in Fig. 1 (b). For the sake of simplicity, we consider only the centrosymmetric slab structure. We also validated that the six QL slab is thick enough to obtain the topologically protected surface bands.

### 2.2 Computational Details

Bandstructure calculations were performed by using a projector augmented wave method<sup>19</sup> implemented in Vienna Ab initio Simulation Package (VASP) code<sup>20</sup> with generalized gradient approximation (GGA)<sup>21</sup> to the density functional theory (DFT). To obtain accurate inter-QL distances, long-range van der Waals interaction was taken into account through semi-empirical corrections by DFT-D2 approach.<sup>22</sup> After the crystal structure was fully optimized until forces acting on atoms were smaller than  $1 \times 10^{-5}$  eV/Å, the spin-orbit coupling was included self-consistently. The  $k$ -point mesh was set to be  $12 \times 12 \times 1$ . The in-plane experimental lattice parameter was used for the calculation; for  $\text{Bi}_2\text{Se}_3$ ,  $\text{Bi}_2\text{Te}_2\text{Se}$ ,  $\text{Bi}_2\text{Te}_3$ ,  $\text{Sb}_2\text{Se}_3$ , and  $\text{Sb}_2\text{Te}_3$ ,  $a = 4.143$ ,<sup>23</sup> 4.280,<sup>24</sup> 4.382,<sup>25</sup> 4.034,<sup>26</sup> 4.250<sup>27</sup> Å were used, respectively. For the hetero-

\*kunihiko@sanken.osaka-u.ac.jp

structural slab calculation, the lattice parameter of the material located at the inner (bulk) part of slab was employed. The vacuum layer was set to be larger than 25 Å between the slabs.

### 3. Results

#### 3.1 Homo-structural TI slabs

First we look at the calculated bandstructures of homo-structural slabs, i.e.,  $(\text{Bi}_2\text{Se}_3)_6$ ,  $(\text{Bi}_2\text{Te}_3)_6$ , and  $(\text{Bi}_2\text{Te}_2\text{Se})_6$  slabs, as shown in Fig. 2 (a)-(c). The band gap of  $(\text{Bi}_2\text{Se}_3)_6$  is calculated as  $E_{\text{gap}}=0.31$  eV, which is consistent with the experimentally measured band gap of bulk  $\text{Bi}_2\text{Se}_3$ ,  $E_{\text{gap}}^{\text{exp}}=0.2-0.3$  eV.<sup>28,29</sup>  $(\text{Bi}_2\text{Te}_3)_6$  shows smaller band gap,  $E_{\text{gap}}=0.27$  eV. Among the three slabs, the band gap is largest,  $E_{\text{gap}} = 0.37$ eV, at  $(\text{Bi}_2\text{Te}_2\text{Se})_6$ . In the slab calculation, the inner four QLs forms the bulk-like bands whereas an outmost QL forms the surface bands. The valence band maximum (VBM) of the bulk QL is found along the  $\bar{\Gamma}-\bar{M}$  path; the conduction band minimum (CBM) is found at the  $\bar{\Gamma}$  point. The spin-polarized Dirac-cone surface states appear at the  $\bar{\Gamma}$  point, while the Dirac point is located only 0.05 eV above the Fermi energy at  $(\text{Bi}_2\text{Se}_3)_6$  and the point is embedded into the valence bands at  $(\text{Bi}_2\text{Te}_2\text{Se})_6$  and  $(\text{Bi}_2\text{Te}_3)_6$ . These electronic structures are apparently not useful for the spintronics applications since the carriers are easily doped into the bulk valence bands and hard to exploit the Dirac carriers. Even worse, the spin current may leak out from the surface to the bulk due to the metallic bulk band structure. Therefore, it is needed to shift the Dirac point upward, away from the VBM to the middle of the energy gap. In order to achieve it, we adopt the following strategy: (1) set four QLs of  $\text{Bi}_2\text{Te}_2\text{Se}$  at the inner (bulk) slab to open the wide bulk band gap and (2) load the surface material which has shallower electron potential onto bulk  $(\text{Bi}_2\text{Te}_2\text{Se})_4$  and make a hetero-structural junction so that the surface state energy is expected to be shifted upward. The computational results of the band-gap and the Dirac cone in the homo-structural TI slabs are summarized in Fig. 3. In the following section, we will present results of hetero-structural slabs as combining two types of TIs.

#### 3.2 $\text{Bi}_2\text{Te}_2\text{Se}$ -based heterostructural TI slab

Following our strategy, several combinations of hetero-structural slabs by using  $\text{Bi}_2\text{Te}_2\text{Se}$  and other TIs were tested. Successful results were obtained only when  $\text{Bi}_2\text{Te}_3$  or  $\text{Sb}_2\text{Te}_3$  was chosen for the surface QL. As shown in Fig. 2 (d), the  $\text{Bi}_2\text{Te}_3/(\text{Bi}_2\text{Te}_2\text{Se})_4/\text{Bi}_2\text{Te}_3$  hetero-structural slab shows the ideal TI surface-band structure, in which the Dirac point is located at the middle of the band gap at the  $\bar{\Gamma}$  point. As compared with the band structure of  $(\text{Bi}_2\text{Te}_2\text{Se})_6$  (cfr. Fig. 2(c)), the bulk band gap is kept large as 0.32 eV, while the Dirac point is shifted upward in energy by 0.19 eV. The effect is simply caused by the replacement of outermost Se layer of the slab by Te layer.

In order to understand the shift of the surface-state energy, we evaluated the work function of slab structures. Table I (upper part) shows the work function  $\phi$  of 6QL slabs that contain a single TI material, where the work function is defined as energy difference between bulk VBM and the potential at the vacuum region between slabs. That can be an indicator of the potential depth of each slab. It can be seen that the work function at  $(\text{Bi}_2\text{Te}_3)_6$ ,  $\phi=4.95$ eV, is slightly shallower than that in  $(\text{Bi}_2\text{Te}_2\text{Se})_6$ ,  $\phi=5.02$ eV. The

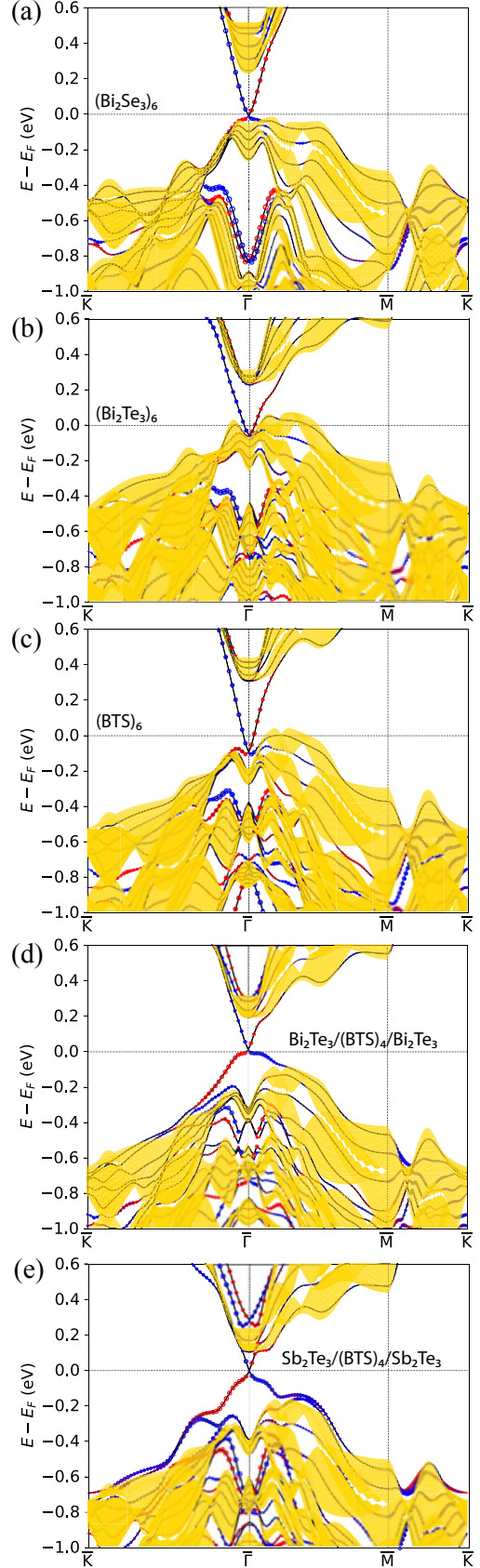


**Fig. 2.** Calculated bandstructure of (a)  $(\text{Bi}_2\text{Se}_3)_6$ , (b)  $(\text{Bi}_2\text{Te}_3)_6$ , (c)  $(\text{Bi}_2\text{Te}_2\text{Se})_6$  (d)  $\text{Bi}_2\text{Te}_3/(\text{Bi}_2\text{Te}_2\text{Se})_4/\text{Bi}_2\text{Te}_3$  and (e)  $\text{Sb}_2\text{Te}_3/(\text{Bi}_2\text{Te}_2\text{Se})_4/\text{Sb}_2\text{Te}_3$  slabs. Red and blue circles indicate the in-plane up and down spin polarization respectively, while the circle size is proportional to the weight contributed from the outermost surface QL. Bulk band projections (bandstructure of bulk crystal, summation of ten slices along  $k_z$ ) are shown by the yellow shade areas.

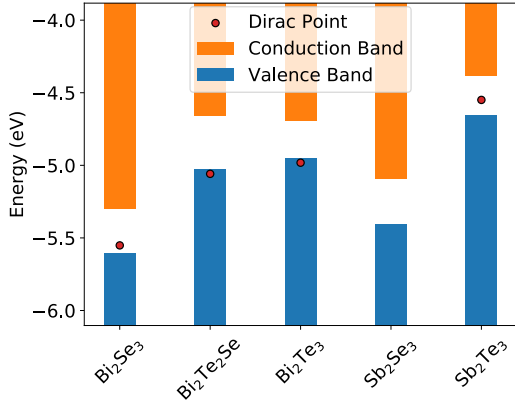


**Fig. 3.** Energy diagram of the bulk valence band maximum and bulk conduction band minimum with respect to the vacuum level, calculated in six QL slab.

difference of these work functions,  $\Delta\phi = +0.07$  eV, is indeed responsible for the upward shift of the Dirac point in  $\text{Bi}_2\text{Te}_3/(\text{Bi}_2\text{Te}_2\text{Se})_4/\text{Bi}_2\text{Te}_3$  multiQL; the surface bands arising from the outmost  $\text{Bi}_2\text{Te}_3$  QL is shifted up relatively to the bulk bands arising from the inner  $(\text{Bi}_2\text{Te}_2\text{Se})_4$  QLs. In the case of a multiQL  $\text{Sb}_2\text{Te}_3/(\text{Bi}_2\text{Te}_2\text{Se})_4/\text{Sb}_2\text{Te}_3$ , as shown in Fig. 2 (e), the Dirac point is shifted further upward by  $\sim 0.003$  eV and approaches the bulk CBM. The trend is also depicted in Fig. 4 (d). This can be understood by calculating the work function at  $(\text{Sb}_2\text{Te}_3)_6$ ,  $\phi = 4.65$  eV, that is smaller than those at  $(\text{Bi}_2\text{Te}_3)_6$  and  $(\text{Bi}_2\text{Te}_2\text{Se})_6$ . The energy difference caused between the surface QL and the inner QLs can be visualized by plotting the electron local potential. Figure 4 (a)-(c) shows the local potential along the out-of-plane axis in a super cell containing 6QL slab and the vacuum region. It is seen that the local potential is rather flat in  $\text{Bi}_2\text{Te}_2\text{Se}$  slab region and becomes shallower at a surface QL of  $\text{Bi}_2\text{Te}_3$  and  $\text{Sb}_2\text{Te}_3$ .

The Dirac surface state is characterized by intriguing properties such as spin-momentum locking caused by lack of space-inversion symmetry and presence of spin-orbit coupling. The isocontour of the surface-band energy and the spin texture of the Dirac surface states in  $\text{Bi}_2\text{Te}_3/(\text{Bi}_2\text{Te}_2\text{Se})_4/\text{Bi}_2\text{Te}_3$  slab are shown in Fig. 5. It is noted that the constant-energy contour of the lower Dirac band shows strongly warped shape (that looks like a snowflake) while the upper Dirac band shows hexagonal-looking energy contour. The difference may come from the different characters of the bands; the upper Dirac band consists of mainly Bi  $p$  orbital state and the lower consists of mainly Te  $p$  state. The warping effect can be also seen in  $\text{Bi}_2\text{Te}_3$  surface,<sup>30)</sup> while the effect is strongly enhanced in  $\text{Bi}_2\text{Te}_3/(\text{Bi}_2\text{Te}_2\text{Se})_4/\text{Bi}_2\text{Te}_3$ , where the outmost  $\text{Bi}_2\text{Te}_3$  surface QL is located between the vacuum region and  $\text{Bi}_2\text{Te}_2\text{Se}$  QLs and create the rather non-centrosymmetric electronic potential at the surface Bi atom. According to a  $k \cdot p$  perturbation theory<sup>30)</sup> with spin-orbit coupling with  $C_{3v}$ -symmetry around the  $\Gamma$  point, effective Hamiltonian up to the third order of  $\vec{k}$  reads

$$H(\vec{k}) = E_0(\vec{k}) + v_k (k_x \sigma_y - k_y \sigma_x) + \frac{\lambda}{2} (k_+^3 + k_-^3) \sigma_z. \quad (1)$$

Here, the first term  $E_0(\vec{k}) = k^2/(2m^*)$  is free-electron dispersion with the mass  $m^*$ . The second term with the Dirac veloc-

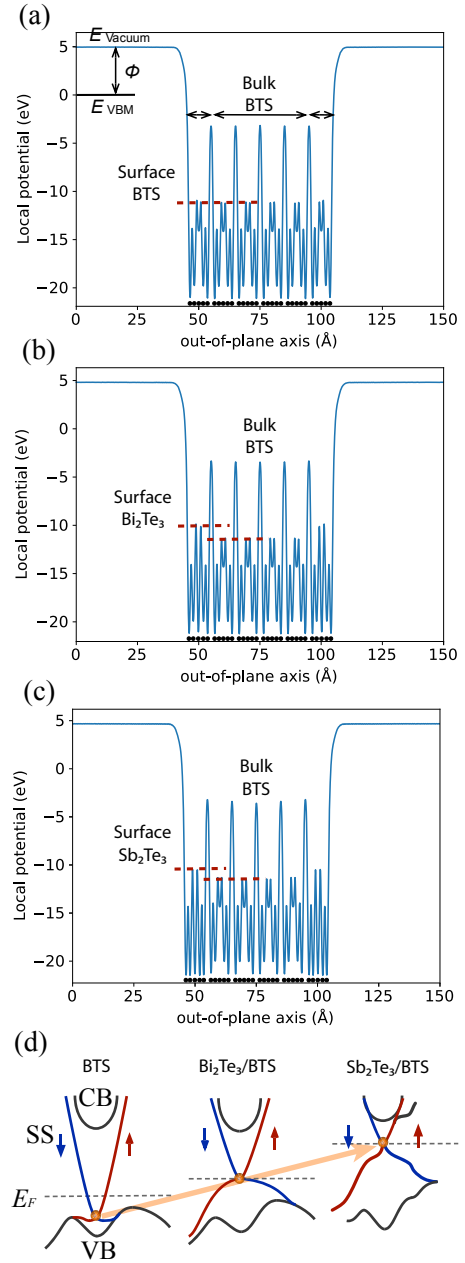


**Fig. 4.** Local potential of (a)  $(\text{Bi}_2\text{Te}_2\text{Se})_6$ , (b)  $\text{Bi}_2\text{Te}_3/(\text{Bi}_2\text{Te}_2\text{Se})_4/\text{Bi}_2\text{Te}_3$ , and (c)  $\text{Sb}_2\text{Te}_3/(\text{Bi}_2\text{Te}_2\text{Se})_4/\text{Sb}_2\text{Te}_3$  slab plotted along the out-of-plane direction. The local potential energy is defined as  $V_{\text{local}} = V_{\text{ionic}} + V_{\text{Hartree}}$  with respect to the  $E_F$  as the origin of energy. Black dots at the graph bottom indicate the atomic position.  $E_{\text{vacuum}}$ ,  $E_{\text{vbm}}$ , and  $\phi$  denote the vacuum energy, the valence energy maximum, and the work function of the slab, respectively. (d) Schematic picture of surface-band states of those slabs.

ity  $v_k = v(1 + \alpha k^2)$  and the in-plane spin momentum  $\sigma_{x,y}$  is responsible for two-dimensional Rashba effect. The last term is essential for the Fermi-line warping (here  $k_{\pm} = k_x \pm ik_y$ ) and also emergence of the out-of-plane spin polarization  $\sigma_z$ . In fact, as shown in Fig. 5 (c), the spin texture of the lower Dirac band shows not only the Rashba-type tangential spin vortex but also the out-of-plane spin component  $S_z$  along the  $\Gamma - \bar{K}$  line away from the  $\Gamma$  point.<sup>31)</sup> The upper and lower bands basically show the opposite directions of spin polarization.

In order to find the optimal Dirac surface state, more than 20 types of hetero-structural topological QL slabs were examined. The calculated results of the

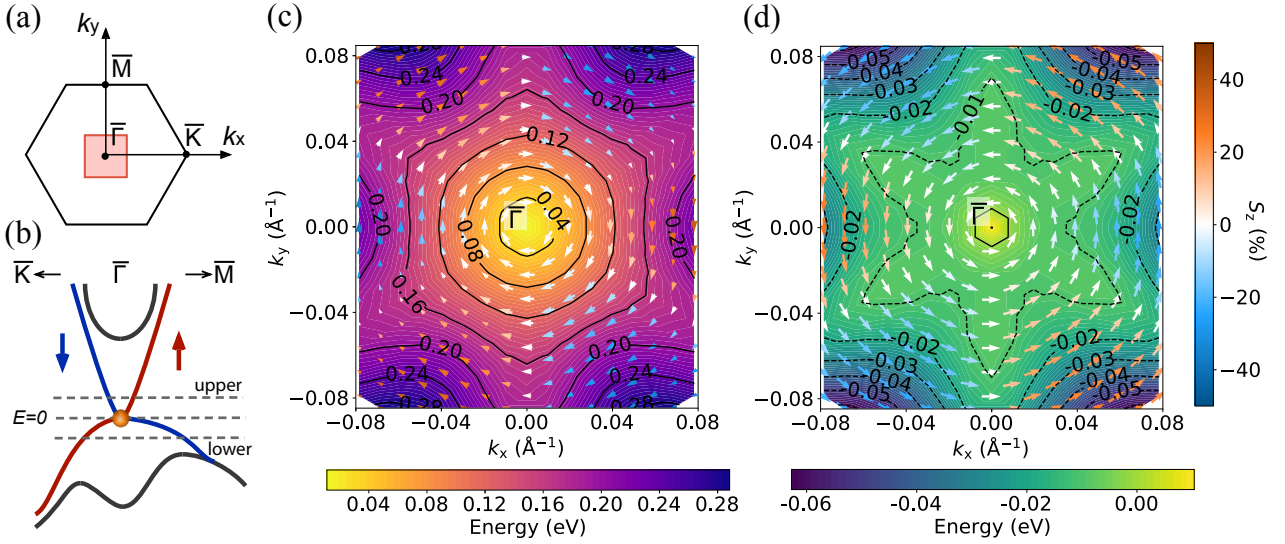


**Fig. 5.** (a) The hexagonal Brillouin zone of  $\text{Bi}_2\text{Te}_3/(\text{Bi}_2\text{Te}_2\text{Se})_4/\text{Bi}_2\text{Te}_3$ . The red square shows the plotting region of spin texture. (b) The schematic band structure of upper and lower Dirac-surface states. Calculated spin texture for (c) the upper Dirac surface band and for (d) the lower Dirac surface band. Lengths and directions of arrows indicate in-plane ( $S_x$ ,  $S_y$ ) spin components. Colors of arrows indicate out-of-plane spin  $S_z$  component. Contours show eigenvalues of Dirac surface bands in each  $k$ -points. Energy is measured with respect to the  $E_F$ .

**Table I.** Calculated band gap of the *bulk* state  $E_{\text{gap}}$ , work function defined as  $\phi = E_{\text{vacuum level}} - E_{\text{Bulk VBM}}$ , and Dirac point energy ( $E_{\text{DP}}$ ) with respect to the *bulk* VBM of the 6QL slabs. Here the *bulk* state is regarded as the state of bands contributed from the inner several QLs in each slab. Position of Dirac point ( $E_{\text{DP}}$ ) in each topological insulators multilayers (Energy from bulk valence band maximum  $E_{\text{Bulk VBM}}$ ).  $a$  is a in-plane lattice constant of each multilayers.  $E_{\text{gap}}$  is a band gap of the bulk states. The bulk states is regarded as the contribution of the bulk layers to the band structure. The bulk layers are inner layers of slabs. Work function  $\phi$  is defined as  $E_{\text{vacuum level}} - E_{\text{Bulk VBM}}$  here. BTS stands for  $\text{Bi}_2\text{Te}_2\text{Se}$ . The ideal  $E_{\text{DP}}$  values (i.e., the Dirac cone appears in the middle of the wide energy gap) are highlighted.

Slab	$E_{\text{gap}}$ (eV)	$\phi$ (eV)	$E_{\text{DP}}$ (eV)
$(\text{Bi}_2\text{Se}_3)_6$	0.305	5.603	+0.052
$(\text{Bi}_2\text{Te}_3)_6$	0.251	4.946	-0.121
$(\text{BTS})_6$	0.366	5.024	-0.091
$(\text{Sb}_2\text{Se}_3)_6$	0.314	5.404	None
$(\text{Sb}_2\text{Te}_3)_6$	0.267	4.650	<b>+0.101</b>
$\text{Sb}_2\text{Se}_3/(\text{Bi}_2\text{Se}_3)_4/\text{Sb}_2\text{Se}_3$	0.269	5.471	+0.016
$\text{Bi}_2\text{Te}_3/(\text{Bi}_2\text{Se}_3)_4/\text{Bi}_2\text{Te}_3$			Metal
$(\text{Bi}_2\text{Te}_3)_2/(\text{Bi}_2\text{Se}_3)_4/(\text{Bi}_2\text{Te}_3)_2$			Metal
$(\text{Sb}_2\text{Te}_3)_2/(\text{Bi}_2\text{Te}_3)_2/(\text{Sb}_2\text{Te}_3)_2$	0.199	4.940	+0.035
$\text{Sb}_2\text{Te}_3/(\text{Bi}_2\text{Te}_3)_4/\text{Sb}_2\text{Te}_3$	0.237	4.949	+0.006
$(\text{Sb}_2\text{Te}_3)_2/(\text{Bi}_2\text{Te}_3)_4/(\text{Sb}_2\text{Te}_3)_2$	0.165	4.891	-0.031
$\text{Bi}_2\text{Se}_3/(\text{Bi}_2\text{Te}_3)_4/\text{Bi}_2\text{Se}_3$			Metal
$(\text{Bi}_2\text{Se}_3)_2/(\text{Bi}_2\text{Te}_3)_4/(\text{Bi}_2\text{Se}_3)_2$			Metal
$\text{Bi}_2\text{Se}_3/(\text{BTS})_4/\text{Bi}_2\text{Se}_3$			Metal
$\text{Bi}_2\text{Te}_3/(\text{BTS})_4/\text{Bi}_2\text{Te}_3$	0.321	4.947	<b>+0.096</b>
$\text{Bi}_2\text{Te}_3/(\text{BTS})_6/\text{Bi}_2\text{Te}_3$	0.290	4.923	<b>+0.113</b>
$(\text{Bi}_2\text{Te}_3)_2/(\text{BTS})_2/(\text{Bi}_2\text{Te}_3)_2$	0.253	4.853	+0.051
$(\text{Bi}_2\text{Te}_3)_2/(\text{BTS})_4/(\text{Bi}_2\text{Te}_3)_2$	0.221	4.817	+0.029
$(\text{Bi}_2\text{Te}_3)_2/(\text{BTS})_6/(\text{Bi}_2\text{Te}_3)_2$	0.172	4.825	+0.038
$(\text{Bi}_2\text{Te}_3)_3/(\text{BTS})_4/(\text{Bi}_2\text{Te}_3)_3$	0.160	4.782	-0.023
$(\text{Bi}_2\text{Te}_3)_3/(\text{BTS})_6/(\text{Bi}_2\text{Te}_3)_3$	0.143	4.806	-0.023
$\text{Sb}_2\text{Se}_3/(\text{BTS})_4/\text{Sb}_2\text{Se}_3$			Metal
$\text{Sb}_2\text{Te}_3/(\text{BTS})_4/\text{Sb}_2\text{Te}_3$	0.265	4.836	<b>+0.158</b>
$\text{Sb}_2\text{Te}_3/(\text{BTS})_6/\text{Sb}_2\text{Te}_3$	0.263	4.830	<b>+0.146</b>
$(\text{Sb}_2\text{Te}_3)_2/(\text{BTS})_2/(\text{Sb}_2\text{Te}_3)_2$	0.225	4.761	+0.150
$(\text{Sb}_2\text{Te}_3)_2/(\text{BTS})_4/(\text{Sb}_2\text{Te}_3)_2$	0.189	4.724	+0.127
$(\text{Sb}_2\text{Te}_3)_2/(\text{BTS})_6/(\text{Sb}_2\text{Te}_3)_2$	0.229	4.664	<b>+0.089</b>
$(\text{Sb}_2\text{Te}_3)_3/(\text{BTS})_4/(\text{Sb}_2\text{Te}_3)_3$	0.136	4.651	+0.050
$(\text{Sb}_2\text{Te}_3)_3/(\text{BTS})_6/(\text{Sb}_2\text{Te}_3)_3$	0.207	4.569	-0.005
$\text{Bi}_2\text{Te}_3/(\text{Sb}_2\text{Te}_3)_2/\text{Bi}_2\text{Te}_3$	0.271	4.685	+0.007

energy gap and the Dirac-point energy are summarized in Table I. Among these heterostructure candidates, the ideal Dirac surface state which form the crossing point at the middle of the wide band gap is found at  $\text{Bi}_2\text{Te}_3/(\text{Bi}_2\text{Te}_2\text{Se})_4/\text{Bi}_2\text{Te}_3$ ,  $\text{Bi}_2\text{Te}_3/(\text{Bi}_2\text{Te}_2\text{Se})_6/\text{Bi}_2\text{Te}_3$ ,  $\text{Sb}_2\text{Te}_3/(\text{Bi}_2\text{Te}_2\text{Se})_4/\text{Sb}_2\text{Te}_3$ ,  $\text{Sb}_2\text{Te}_3/(\text{Bi}_2\text{Te}_2\text{Se})_6/\text{Sb}_2\text{Te}_3$ , and  $(\text{Sb}_2\text{Te}_3)_2/(\text{Bi}_2\text{Te}_2\text{Se})_6/(\text{Sb}_2\text{Te}_3)_2$ . In these slabs, as discussed above, the bulk  $\text{Bi}_2\text{Te}_2\text{Se}$  QLs opens the wide band gap ( $E_{\text{gap}} \sim 0.3$  eV) and the surface Dirac cone originating from  $\text{Bi}_2\text{Te}_3$  and  $\text{Sb}_2\text{Te}_3$  QLs appears at the middle of the gap; the shallower work function of the surface QL with respect to that of the bulk QL slightly shifts up the surface state energy; e.g.,  $(\text{Sb}_2\text{Te}_3)_6$  slab shows  $\phi = 4.95$  eV and  $(\text{Bi}_2\text{Te}_2\text{Se})_6$  shows  $\phi = 5.02$  eV. As varying the number of  $\text{Sb}_2\text{Te}_3$  and  $\text{Bi}_2\text{Te}_2\text{Se}$  QLs at  $(\text{Sb}_2\text{Te}_3)_n/(\text{Bi}_2\text{Te}_2\text{Se})_m/(\text{Sb}_2\text{Te}_3)_n$  slabs, it is feasible to tune the position of the Dirac cone in the wide energy region ( $0 < E_{\text{DP}} < 0.16$ ). On the other hand, when we combine two types of QL-materials whose work functions are much different, the hetero-structural slab goes metallic. For example, the  $\text{Bi}_2\text{Se}_3$  and  $\text{Bi}_2\text{Te}_3$  6QL slabs show  $\phi = 5.60$  and 4.95 eV, respectively, and then the hetero-structural combination of these QLs is found to be metallic. In  $(\text{Bi}_2\text{Te}_3)_n/(\text{Bi}_2\text{Se}_3)_m/(\text{Bi}_2\text{Te}_3)_n$  slabs, it is metallic not only at the surface state but also at the bulk state because the CBM of  $\text{Bi}_2\text{Se}_3$  overlaps with the VBM of  $\text{Bi}_2\text{Te}_3$  (see Fig. 3).

#### 4. Summary

First-principles DFT calculations have been carried out on the hetero-structural multi-QL slabs of topological insulators. We have demonstrated that the Dirac-point position can be shifted to the middle of the band gap by combining the appropriate pair of QLs of different materials. The surface-band energy can be further tuned by varying the number of QLs in the slab. Since the controllability of Dirac cone can be acquired by simple combination of the conventional topological insulators, it may be easily confirmed by following experimental studies and promising for future spintronics applications.

KY acknowledges Takafumi Sato and Seigo Souma for the fruitful discussions on topological materials. This work was supported by JSPS Kakenhi (No. 17H02916 and 18H04227) and by JST-CREST (No: JPMJCR18T1). A part of the computation in this work has been done by using the facilities of the Supercomputer Center, the Institute for Solid State Physics, the University of Tokyo. The crystallographic figure was generated using VESTA program.<sup>32)</sup>

- 1) M. Z. Hasan and C. L. Kane, *Rev. Mod. Phys.* **82**, 3045 (2010) .
- 2) X.-L. Qi and S.-C. Zhang, *Rev. Mod. Phys.* **83**, 1057 (2011).
- 3) Y. Xia, D. Qian, D. Hsieh, L. Wray, A. Pal, H. Lin, A. Bansil, D. Grauer, Y. S. Hor, R. J. Cava and M. Z. Hasan, *Nature Phys.* **5**, 398 (2009).
- 4) J. E. Moore, *Nature (London)* **464**, 194 (2010).
- 5) D. O. Scanlon, P. D. C. King, R. P. Singh, A. de la Torre, S. M. Walker, G. Balakrishnan, F. Baumberger, and C. R. A. Catlow, *Adv. Mater.* **24**, 2154 (2012) .
- 6) L.-L. Wang, M. Huang, S. Thimmaiah, A. Alam, S. L. Budko, A. Kaminiski, T. A. Lograsso, P. Canfield, and D. D. Johnson, *Phys. Rev. B* **87**, 125303 (2013) .
- 7) N. P. Butch, K. Kirshenbaum, P. Syers, A. B. Sushkov, G. S. Jenkins, H. D. Drew, and J. Paglione, *Phys. Rev. B* **81**, 241301 (2010).
- 8) J. G. Analytis, J.-H. Chu, Y. Chen, F. Corredor, R. D. McDonald, Z. X. Shen, and I. R. Fisher, *Phys. Rev. B* **81**, 205407 (2010).
- 9) K. Eto, Z. Ren, A. A. Taskin, K. Segawa, and Y. Ando, *Phys. Rev. B* **81**, 195309 (2010) .
- 10) D.-X. Qu, Y. S. Hor, J. Xiong, R. J. Cava, and N. P. Ong, *Science* **329**, 821 (2010).
- 11) Y. Xia, D. Qian, D. Hsieh, L. Wray, A. Pal, H. Lin, A. Bansil, D. Grauer, Y. S. Hor, R. J. Cava, and M. Z. Hasan, *Nat. Phys.* **5**, 398 (2009).
- 12) Y. L. Chen, J. G. Analytis, J.-H. Chu, Z. K. Liu, S.-K. Mo, X. L. Qi, H. J. Zhang, D. H. Lu, X. Dai, Z. Fang, S. C. Zhang, I. R. Fisher, Z. Hussain, and Z.-X. Shen, *Science* **325**, 178 (2009).
- 13) D. Hsieh, Y. Xia, D. Qian, L. Wray, F. Meier, J. H. Dil, J. Osterwalder, L. Patthey, A. V. Fedorov, H. Lin, A. Bansil, D. Grauer, Y. S. Hor, R. J. Cava, and M. Z. Hasan, *Phys. Rev. Lett.* **103**, 146401 (2009).
- 14) Z. Ren, A. A. Taskin, S. Sasaki, K. Segawa, and Y. Ando, *Phys. Rev. B* **8**, 155301 (2012).
- 15) J. Xiong, A. C. Petersen, D. Qu, Y. S. Hor, R. J. Cava, and N. P. Ong, *Physica E* **44**, 917 (2012).
- 16) Z. Ren, A. A. Taskin, S. Sasaki, K. Segawa, and Y. Ando, *Phys. Rev. B* **82**, 241306(R) (2010).
- 17) T. Arakane, T. Sato, S. Souma, K. Kosaka, K. Nakayama, M. Komatsu, T. Takahashi, Z. Ren, K. Segawa, and Y. Ando, *Nature Commun.* **3**, 636 (2012).
- 18) A. A. Taskin, Z. Ren, S. Sasaki, K. Segawa, and Y. Ando, *Phys. Rev. Lett.* **107**, 016801 (2011).
- 19) P. E. Blöchl, *Phys. Rev. B* **50**, 17953 (1994).
- 20) G. Kresse, J. Furthmüller, *Phys. Rev. B* **54**, 11169 (1996).
- 21) J. P. Perdew, K. Burke and M. Ernzerhof, *Phys. Rev. Lett.* **77**, 3865 (1996).
- 22) S. Grimme, *J. Comput. Chem.* **27**, 1787 (2006) .
- 23) S. Nakajima, *J. Phys. Chem. Solids* **24**, 479 (1963).
- 24) J. A. Bland and S. J. Basinski, *Can. J. Phys.* **39**, 1040 (1961).
- 25) Y. Miyazaki and T. Kajitani, *J. of Crys. Growth*, **229**, 542 (2001).
- 26) Since the experimental lattice constants for Sb<sub>2</sub>Se<sub>3</sub> were not found in literatures, the lattice structure was obtained by lattice optimization.
- 27) R. W. G. Wyckoff, *Crystal Structures 2* (Wiley, New York, 1964); Th. L. Anderson, H. Krause and H. Brigitte, *Acta Crystallogr. B* **30**, 1307 (1974).
- 28) I. A. Nechaev et al., *Phys. Rev. B* **87**, 121111 (2013).
- 29) G. Martinez et al., *Sci Rep.* **7**, 6891 (2017).
- 30) L. Fu, *Phys. Rev. Lett.* **103**, 266801 (2009).
- 31) S. Souma, K. Kosaka, T. Sato, M. Komatsu, A. Takayama, T. Takahashi, M. Kriener, K. Segawa, and Y. Ando, *Phys. Rev. Lett.* **106**, 216803 (2011).
- 32) K. Momma and F. Izumi, *J. Appl. Crystallogr.* **44**, 1272 (2011).